Iterative Reconstruction Methods for Nonuniform Attenuation Distribution in SPECT

Anne Maze, Joseph Le Cloirec, René Collorec, Yves Bizais, Philippe Briandet and Patrick Bourguet

Inserm U 335, Centre Eugène Marquis, Rennes, France; Sopha Médical, Buc, France and CHU, Nantes, France

Two iterative methods, a generalization of the Chang method and a projection precorrection, were investigated to determine whether the use of an attenuation map could improve nonuniform attenuation compensation. After a detailed description of the methods, results obtained with simulated and phantom data were compared. This study demonstrates that projection precorrection provides accurate quantification and good image quality as early as the precorrection step, whereas the generalized Chang method requires computation of one more iteration.

J Nucl Med 1993; 34:1204–1209

Several correction methods addressing the fundamental problem of photon attenuation compensation in quantitative image reconstruction have been described in the literature (*1–3*), assuming, however, that uniform attenuation reduces the validity of the correction in nonhomogeneous regions and thus places limitations on the correction methods. Therefore, in order to ensure proper correction, density distribution must be determined in nonhomogeneous regions (*4,5*). This can be obtained with a map of body attenuation coefficients produced by transmission studies using a radioactive flood source mounted on the scintillation camera (*6,7*). When the collimator functions in parallel geometry, the map produced is very noisy, with poor spatial resolution. Inversely, if the collimator operates with cone-beam geometry, which gives better detection sensitivity, a good quality image is produced (*8*). Good image quality can also be achieved with x-ray computed tomography (CT) (*9*), but CT and single-photon emission computed tomography (SPECT) images must be superimposed to produce the correction map. Precise alignment requiring interpolation is difficult to obtain and can be a source of error, especially since SPECT views have lower resolution and imprecise anatomical landmarks. The approximations made in deriving the relationship between the CT number in Hounsfield's units and the linear attenuation coefficient for SPECT radionuclides can also lead to errors. Since little is known about the effect of such errors, we conducted this study to investigate how they affect quantitative accuracy in SPECT reconstruction.

Received Aug. 19, 1992; revision accepted Feb. 8, 1993.

For correspondence or reprints contact: Patrick Bourguet, MD, PhD, Service de Médecine Nucléaire, Centre Eugène Marquis, BP 6279, 35062 Rennes Cedex, France.

METHODS

Attenuation Correction Algorithms

Two iterative algorithms have been developed based on filtered backprojection, both correcting for nonhomogeneous attenuation in density maps incorporated into emission data.

Generalized Chang Correction. Chang's traditional iterative algorithm (*1*), the method most often cited in the literature, has been generalized for nonuniform attenuation by several authors (*10*) and is referred to here as the generalized Chang correction (GCC). This algorithm is based on measurements of the body contour and assumes a constant linear attenuation coefficient (*1*). We used the Chang compensation method in its iterative form and generalized it for nonuniform attenuation. In this form, each pixel value in the initial filtered backprojection reconstruction (Hann's filter) is multiplied by a correction term c(i, j) which is related to the average attenuation for that pixel. This term can be written as:

$$c(i, j) = \frac{1}{\frac{1}{M}\sum_{k=1}^{M} \exp\left(-\sum_{i'=i}^{N} \mu i', jd\right)}, \qquad \text{Eq. 1}$$

where M is the number of angles equal to the number of views, N is the number of pixels on the line of the image, $\mu_{i,j}$ is the attenuation coefficient distribution and d is pixel length.

Following the first order correction described above, a second order correction was obtained by applying one further processing step, and the first order corrected image was reprojected to model attenuation based on the map's attenuation distribution. Error projections were then obtained by subtracting the new reprojected data from the original data. An error image was reconstructed and multiplied by the correction matrix. The second order corrected image was finally obtained by adding the corrected error image to the first order image reconstructed previously. The n^{th} order corrected image was obtained by repeating the procedure n times.

Iterative Precorrection Method. In the second method, iterative precorrection (IPC), multiplying factors, $F_{\theta j}$, were applied to measured projections before backprojection of the original data $P_{\theta j}$. These factors were calculated from the attenuation map coefficients. Each factor was equal to the reciprocal of the average attenuation along the projection ray through the section of the patient:

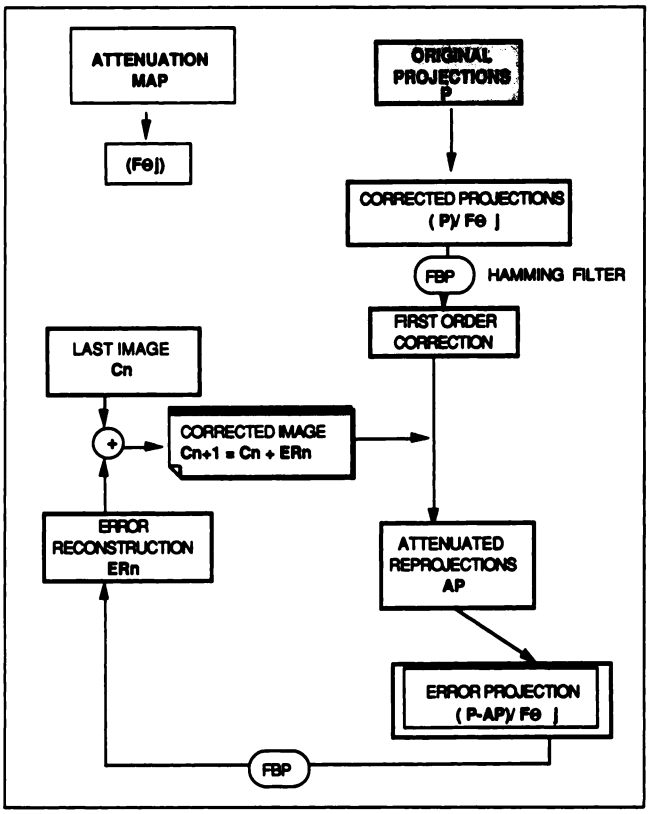

FIGURE 1. Algorithm of the IPC method. FBP = Filtered backprojection.

$$F_{\theta j} = \frac{1}{\frac{1}{N}\sum_{i=0}^{N}\left(\exp\left(-\sum_{i'=i}^{N}\mu_{i'jd}\right)\right)}, \qquad \text{Eq. 2}$$

where N is the number of pixels in the section of the object along the projection ray. The expression of the corrected projections is:

$$Pc_{\theta j} = \frac{P_{\theta j}}{F_{\theta j}}, \qquad \text{Eq. 3}$$

where $P_{\theta j}$ is the count density at the pixel j of the line projection at angle θ.

The algorithm is shown in Figure 1. The corrected projections were filtered with a Hann's filter and backprojected. A second order correction was obtained by applying one additional processing step to compute a new set of projections based on the map's attenuation coefficients. Error projections were then computed and corrected with the multiplying factors, filtered and backprojected. The error image obtained was added to the first order correction to obtain the first iteration. The same procedure was repeated in order to improve reconstruction.

Mapping Technique

Since the methods described above require the alignment of the CT and SPECT images, we developed a map obtained from CT images aligned to the corresponding SPECT slices with markers based on a relationship converting Hounsfield's units to SPECT radionuclide attenuation coefficients for a 140-keV photon (^{99m}Tc). External metal markers injected with ^{131}I were used and double-energy window SPECT was performed. The CT images were aligned on the SPECT images using the position of the markers. The transformation was assumed to be polynomial (*11*). To obtain the relationship between the CT number N_{CT} and the attenuation coefficient for a 75-keV mean energy x-ray beam, we measured the CT number of different materials of known attenuation on a CT Scanner (CE 10000, General Electric, Milwaukee, WI). This procedure gave a linear equation:

$$\text{at 75 keV:} \quad \mu(cm^{-1}) = 1.89\ 10\text{-}4\ (N_{CT}) + 0.1845. \qquad \text{Eq. 4}$$

An analysis of the mass attenuation coefficients for various body materials has indicated that it should be possible to multiply the linear attenuation coefficient determined at 75 keV by a conversion factor to obtain the value at 140 keV (^{99m}Tc energy) (*12*). For soft tissue, this factor has been estimated to be 0.853, with a maximal relative error of 5% (*13,14*). A different value has been obtained for bone. We therefore developed a phantom with attenuation material equivalent to soft tissue. The conversion relationship thus applied to the CT images was:

$$\text{at 140 keV:} \quad \mu(cm^{-1}) = 1.578\ 10\text{-}4\ (N_{CT}) + 0.157. \qquad \text{Eq. 5}$$

Data published earlier support the application of these methods to in vivo human studies (*15*). This conversion was applied to the CT images and gave linear attenuation coefficients in good agreement with published data.

Simulation Model

In order to compare the effectiveness of both attenuation compensation algorithms, a thorax simulation model was developed. Figure 2 shows the activity (ρij in cps) and attenuation coefficient distributions (μij in cm^{-1}) in the model digitized in 64 × 64 matrices. Attenuation coefficients ranged from 0.03 cm^{-1} in simulated lung tissue to 0.2 cm^{-1} in simulated bone. Data acquisition was simulated for a rotating gamma camera system. Projection ray

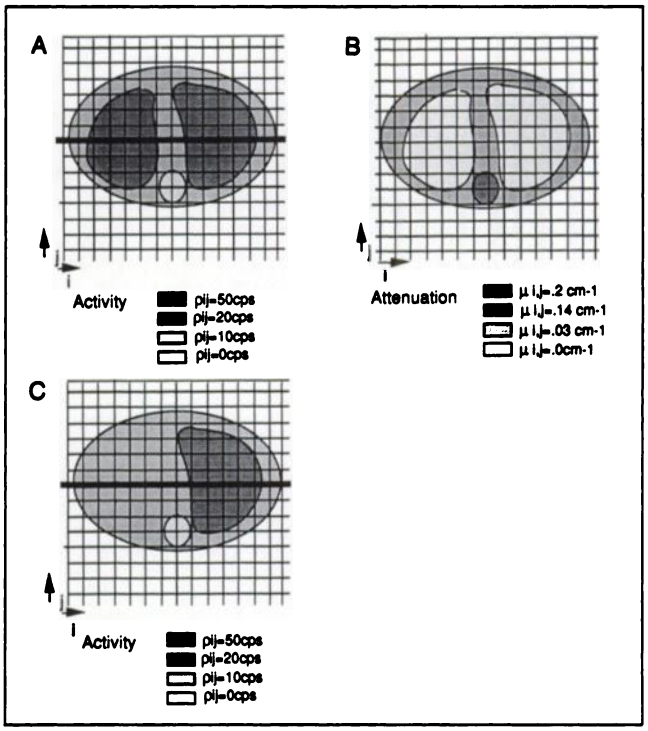

FIGURE 2. Simulation model. Activity distribution (top left (A) and bottom (C)) and attenuation distribution (B, right). The activity profiles are drawn for the horizontal sections shown on the left.

sums were calculated from the activity distribution shown in Figure 2A for 64 equally spaced angles over 360°. The attenuation coefficient distribution shown in Figure 2B was used to simulate the attenuated projections described in the equation given below (*6*). The intersection of the projection ray with each pixel for an angle, θ, was computed (*16*). The calculated data included the effect of attenuation. Compton scattering and collimator and camera responses were not taken into account. The value of the ray-sum j_0 of the projection at angle θ is:

$$p(\theta, j_0) = \sum_{i=1}^{64} \rho_{ij_0} \exp\left(- \sum_{i'=i}^{64} d\mu_{i'j_0} \right). \qquad \text{Eq. 6}$$

In order to evaluate quantitative accuracy, an ideal attenuation map was simulated and incorporated into both algorithms. The attenuation coefficients used for this nonuniform attenuation map were chosen according to the published data: 0.03 cm^{-1} for lungs, 0.2 cm^{-1} for the spine and 0.14 cm^{-1} for other tissues (Fig. 2B). A uniform map was generated in order to compare routinely used uniform attenuation correction with nonuniform correction. A constant coefficient was assigned to each pixel inside the contour of the object. A value of 0.07 cm^{-1} was obtained by computing the average of the attenuation distribution within the ideal map.

We evaluated the effect on reconstruction due to variations of the attenuation map. Different nonuniform maps were computed: with overestimation or underestimation of the attenuation coefficients done while the Hounsfield's values were converted with misalignment on the emission image and with different levels of noise. In order to evaluate the accuracy, the root normalized error (RNE) value was calculated:

$$RNE = \sqrt{\frac{\sum_i \sum_j (\rho_{i,j} - F_{i,j})^2}{\sum_i \sum_j \rho_{i,j^2}}}, \qquad \text{Eq. 7}$$

where $\rho_{i,j}$ and $F_{i,j}$ are, respectively, the simulated and the reconstructed activities at pixel (i,j).

In order to test the attenuation correction methods when the activity level is not symmetrically distributed, we modified the thorax simulation phantom shown in Figure 2. In this second simulation, the distribution remained unchanged, while the activity of the right lung was reduced from 50 to 20 counts per pixel per second, which corresponds to the level of activity in the mediastinum (Fig. 2C).

Phantom Study

The mapping technique and both attenuation correction methods were then applied to real data obtained from a nonuniform attenuation phantom filled with ^{99m}Tc activity.

The phantom consisted of a cylindrical 22-cm diameter container which was used to simulate the thorax. Two cylindrical 6.5-cm diameter polystyrene blocks were placed inside the phantom to simulate lung attenuation. Because water simulates the attenuation of soft tissue, the space between the polystyrene blocks was filled with water containing 600 MBq of ^{99m}Tc. SPECT acquisition was carried out using a SOPHY DSX camera (Sopha Medical, France) equipped with a medium-energy collimator. To enable subsequent alignment of SPECT and CT images, four sets of three markers injected with ^{131}I were taped to the phantom. Two sets of 64 projections were acquired simultaneously in both energy windows (140 keV for ^{99m}Tc and 360 keV for ^{131}I). The acquisition time was 10 sec/projection. Images were stored in 128 × 128 matrices. Each set of projections was filtered and backprojected. Reconstruction with the markers was used for CT alignment. Twenty CT images were acquired (CE10000; G.E.) at 120 kV (corresponding to a beam of 75 keV mean energy). The slice thickness was 1 cm. The CT slices were aligned on the SPECT images using the alignment method described above. The next step in the calculation was to convert Hounsfield's units to attenuation coefficients as described previously. This attenuation map was then used to provide attenuation correction with the methods described above.

Activity profiles were drawn through the center of the reconstructed image and compared with the theoretical profile. An estimation of the detectability of a cold region was provided by the contrast factor:

$$C = (R-B)/B, \qquad \text{Eq. 8}$$

where R is the mean value per pixel in the cold region and B is the mean value per pixel in a background region. The contrast factor varied between −1 for optimal contrast and 0 for minimal contrast in the cold regions ($\rho = 0$).

RESULTS

Simulation Study

Figure 3a shows the results obtained from filtered backprojection without attenuation correction. The horizontal activity profile was compared with the theoretical profile. Count density was totally lost between the lungs. The first order correction of the GCC method did not give a satisfactory image. The activity in the mediastinum was totally lost as in the noncorrected image (Fig. 3b), but within the lungs the activity level was nearly the same as the theoretical distribution. One iteration was required to obtain the true activity throughout the entire image, but the profile showed that iteration added noise (Fig. 3c). As early as the first order correction of the IPC method, the activity distribution was close to the true distribution throughout the image (Fig. 3d). One iteration improves compensation without adding noise (Fig. 3e). Identical results have been obtained with asymmetrical activity distribution (Fig. 4).

Due to the discrete process and the interpolation done in the computation of the projections, these projections did not match exactly with the Radon transform, in contrast to filtered backprojection which is an exact analytical inversion of the Radon transform. Thus, even in the theoretical case of no attenuation, an RNE error of 15% was introduced into the reconstructed image. Figure 5 shows a dramatic improvement in both the GCC and IPC methods when nonuniform attenuation information was introduced. When the ideal attenuation map was used, both methods converged rapidly to an error value of 12%. One iteration was required to improve reconstruction with the GCC method due to high RNE at precorrection. With the IPC method, good accuracy was already obtained at the precorrection step.

Approximate assumptions which could lead to systematic overestimation or underestimation of the attenuation coefficients throughout the object had to be made in order

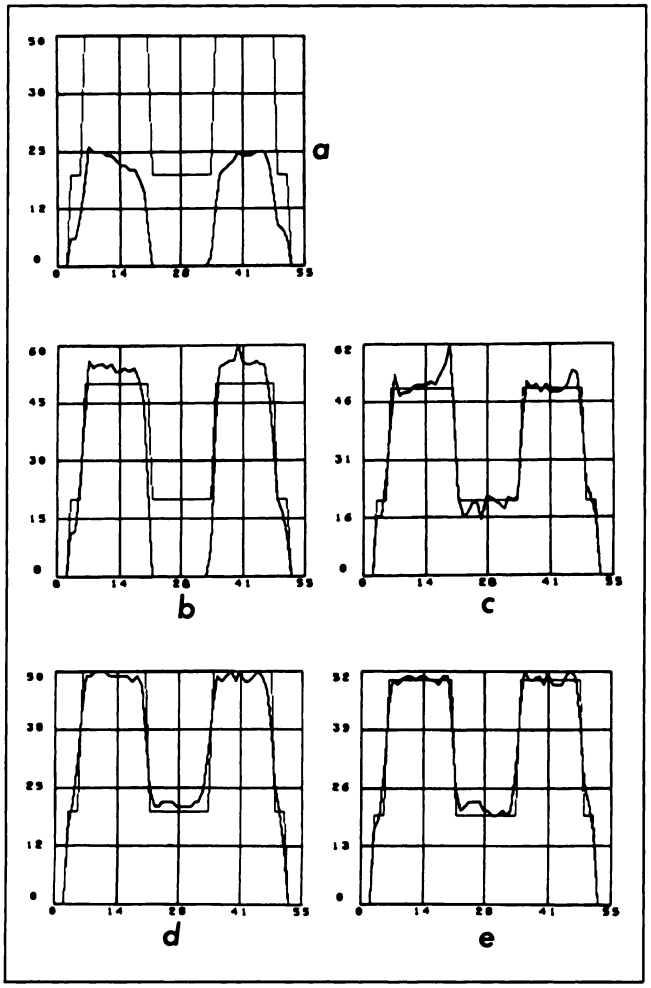

FIGURE 3. Simulation results for symmetrical activity distribution and comparison of activity and theoretical profiles. (A) Filtered backprojection; (B) precorrection of the GCC method; (C) iteration one of the GCC method; (D) precorrection of the IPC method; and (E) iteration one of the IPC method.

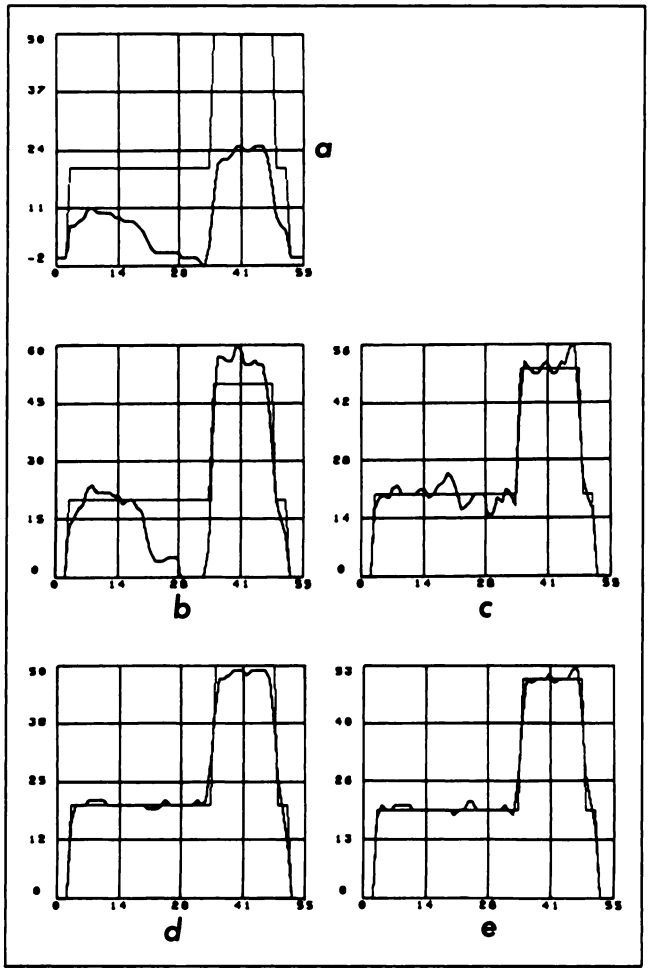

FIGURE 4. Simulation results for asymmetrical activity distribution and comparison of activity and theoretical profiles. (A) Filtered backprojection; (B) precorrection of the GCC method; (C) iteration one of the GCC method; (D) precorrection of the IPC method; and (E) iteration one of the IPC method.

to convert the Hounsfield's units to attenuation coefficients for radionuclide photons. Different nonuniform attenuation maps were simulated increasing or decreasing all the coefficients by 10% or 20% of the true values. With the IPC method, overestimation or underestimation resulted in systematic overestimation or underestimation of the activity levels. With the GCC method, the images were noisy. The RNE were not significantly different between the two methods (Fig. 6A). A 10% overestimation did not lead to significant quantification error. With 20% overestimation, the RNE was sometimes more than 20%. The accuracy of the conversion method used was evaluated at 5%, and so did not lead to significant error in quantification.

Errors due to misalignment of the nonuniform attenuation map on the SPECT image were evaluated by shifting the attenuation map one and two pixels to the left or to the right in the horizontal direction (1 pixel = 6 mm, that is, 1/50th of the simulated thorax). The corrected images were distorted at the frontier between the different tissues. The RNE at iteration one for the GCC method and at precorrection for the IPC method were not significantly different (Fig. 6B). Depending on the alignment error, the RNE was higher either for the IPC or for the GCC method. Error was significant when the map had been shifted by two pixels, which strongly distorted the image. The precision of the

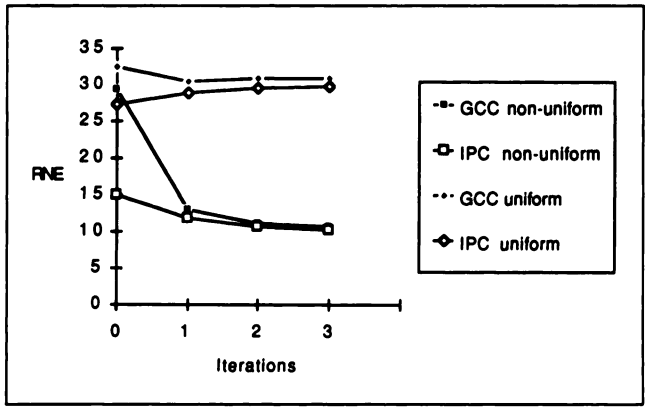

FIGURE 5. Comparison of uniform and nonuniform attenuation correction. The constant value for uniform correction is 0.07 cm^{-1}.

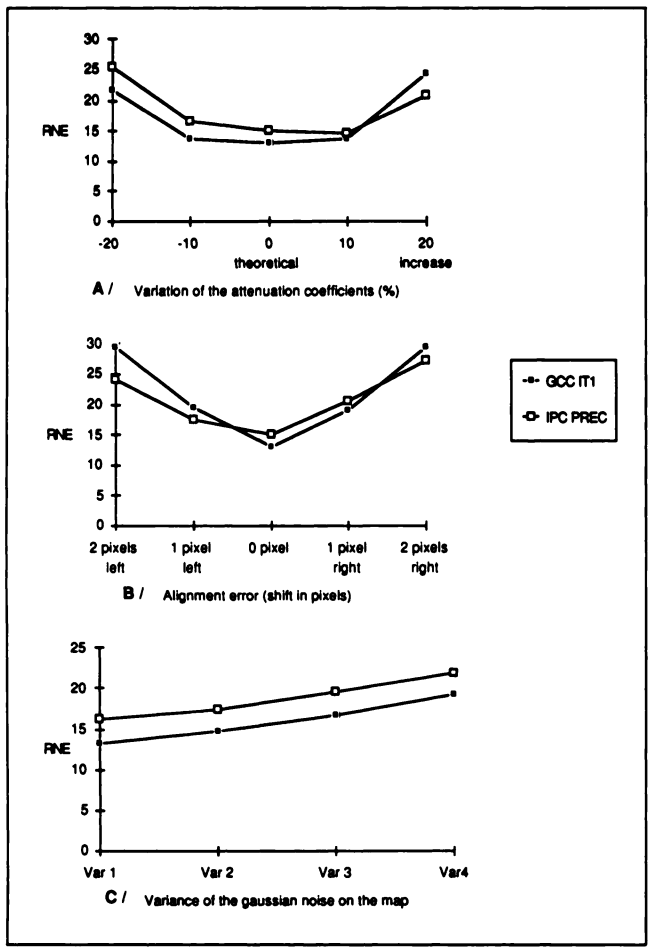

FIGURE 6. Effect on reconstruction due to variations of the attenuation map. Iteration one of the GCC method is compared with the precorrection step of the IPC method. (A) Influence of variation in attenuation coefficients. Variation in percent of the ideal value. (B) Effect of misaligning CT images on SPECT images. (C) Effect of Gaussian noise on the attenuation map.

alignment algorithm was evaluated to be one pixel for a rigid object, although the error was sometimes greater for the thorax.

In order to evaluate the effect of a noisy attenuation map on the corrected image, maps were computed with different variances of Gaussian noise. Figure 6C shows the RNE of both methods at iteration one of GCC and precorrection of IPC for different variances. RNE was higher at the IPC precorrection. The level of noise on CT images was low (var = 1) and did not lead to significant quantification errors.

Phantom Study

Linear attenuation coefficients were obtained from CT acquisition. The values were in good agreement with the literature. The SPECT image was reconstructed using the filtered backprojection method without attenuation correction and both iterative attenuation correction algorithms. After usual backprojection with a Hann's filter, we noticed a dramatic loss of counts, particularly at the center of the image. Cold cylinder regions sometimes appeared active. With first order GCC correction, counts in those regions remained high. One iteration was required to improve resolution and to remove the incorrect counts in the cold regions, but noise increased concurrently. Precorrection of the IPC improved the results because very few counts were reconstructed in the cold regions. Stronger contrast was apparent. One iteration resulted in little improvement at the center.

Contrast was evaluated in the cold region of the phantom, which was poor after filtered backprojection (C = 0) and did not improve in the first order GCC correction (C = −0.6). It did increase after one iteration (C = −0.83), but noise also increased simultaneously. In the precorrection step of the IPC method, contrast was close to the ideal value (C = −1) and did not move after one iteration (C = −1).

DISCUSSION

It has been shown that the GCC algorithm leads to good results in terms of contrast and quantification after one iteration at the expense of a higher noise level. IPC performs better and does not need to be iterated. The attenuated corrected image depends on the quality of the map. We have shown how these algorithms are affected by attenuation map-related errors. When misalignment was greater than one pixel, the corrected image was strongly distorted. Overestimations or underestimations of the coefficients did not distort the images, but did affect quantitative accuracy. The Chang reconstructed image was always more noisy than the IPC image. When the map used was very noisy, the reconstruction images were also noisy. IPC images were affected the most.

This study enabled us to evaluate the precision of the map needed to obtain good image reconstruction. With the mapping technique described in this study, alignment precision was one pixel and the conversion relationship varied within 5%. Noise variance was not greater than one. The results show that the IPC and GCC methods are largely unaffected by such errors. In all cases, the level of accuracy was the same at GCC iteration one and at IPC precorrection.

Theoretically, source distribution could be adequately quantified using iterative reconstruction algorithms with a projector-backprojector that correctly models attenuation, Compton scattering and resolution degradation due to source depth. The above methods could be extended by integrating all these factors dealing with cone-beam geometry instead of parallel geometry. When compared with iterative EM algorithms (*17–19*), these methods require a reduced number of iterations and low computation resources; they are therefore potentially more practical for routine clinical application.

Computation time is one of the most important considerations in assessing algorithms for routine clinical use. Our reconstruction times on the Sophy computer should be used only for comparison, since our software was not

optimized in any way for speed. The computation of the Chang correction matrix or of the IPC correction factors required 1 min per slice, as did computation of the attenuated reprojections at each slice iteration. Since the IPC method achieves good accuracy as early as the precorrection stage, this method is twice as fast as the GCC method, which requires one more iteration computation.

REFERENCES

1. Chang LT. A method for attenuation correction in radionuclide computed tomography. *IEEE Trans Nucl Sci* 1978;25:638–643.
2. Walters TE, Simon W, Chesler DA, Correia JA. Attenuation correction in gamma emission computed tomography. *J Comp Assist Tomogr* 1981;5:89–94.
3. Tanaka E. Quantitative image reconstruction with weighted backprojection for single photon emission computed tomography. *J Comp Assist Tomogr* 1983;7:692–700.
4. Manglos SH, Jaszczak RJ, Floyd CE, Hahn LJ, Greer KL, Coleman RE. Nonisotropic attenuation in SPECT: phantom tests of quantitative effects and compensation techniques. *J Nucl Med* 1987;28:1584–1591.
5. Tsui BMW, Gullberg GT, Edgerton ER, et al. Correction of nonuniform attenuation in cardiac SPECT imaging. *J Nucl Med* 1989;30:497–507.
6. Malko JA, Van Heertum GT, Gullberg GT, Kowalsky WP. SPECT liver imaging using an iterative attenuation correction algorithm and an external flood source. *J Nucl Med* 1986;27:701–705.
7. Flemming JS. A technique for using a CT image in attenuation correction and quantification in SPECT. *Nucl Med Commun* 1989;10:83–87.
8. Manglos SH, Bassano DA, Duxbury CE, Capone RB. Attenuation maps for SPECT determined using cone beam transmission computed tomography. *IEEE Trans Nucl Sci* 1990;37:600–608.
9. Bailey DL, Hutton BR, Walker PJ. Improved SPECT using simultaneous emission and transmission tomography. *J Nucl Med* 1987;28:844–851.
10. Gilland DR, Jaszczak RJ, Greer KL, Coleman RE. Quantitative SPECT reconstruction of iodine-123 data. *J Nucl Med* 1991;32:527–533.
11. Gerlot P, Bizais Y. Image registration: a review and a strategy for medical applications. *Inf Proc Med Imaging* 1988:81–91.
12. McCullough EC. Factors affecting the use of quantitative information from a CT scanner. *Radiology* 1977;124:99–107.
13. Nickoloff EL, Perman WH, Esser PD, Bashist B, Alderson PO. Left ventricular volume: physical basis for attenuation corrections in radionuclide determination. *Radiology* 1984;152:511–515.
14. Rowell NP, Glaholm J, Flower MA, Cronin B, McCready VR. Anatomically derived attenuation coefficients for use in quantitative single photon emission tomography studies of the thorax. *Eur J Nucl Med* 1992;19:36–40.
15. Rao PS, Gregg EC. Attenuation of monoenergetic gamma rays in tissues. *Radiology* 1975;123:631–637.
16. Gullberg GT, Huesman RH, Malko JA, Pelot NJ, Budinger TF. An attenuated projector-backprojector for iterative SPECT reconstruction. *Phys Med Biol* 1985;8:799–816.
17. Miller MI, Snyder DL, Miller TR. Maximum likehood reconstruction for single photon emission computed tomography. *IEEE Trans Nucl Sci* 1985; NS-32:769–778.
18. Lange K, Carson R. EM reconstruction algorithms for emission and transmission tomography. *J Comp Assist Tomogr* 1984;8:306–316.
19. Shepp LA, Vardi Y. Maximum likelihood reconstruction for emission tomography. *IEEE Trans Med Imag* 1982;MI-1:113–122.